General Disclaimer

One or more of the Following Statements may affect this Document

- This document has been reproduced from the best copy furnished by the organizational source. It is being released in the interest of making available as much information as possible.

- This document may contain data, which exceeds the sheet parameters. It was furnished in this condition by the organizational source and is the best copy available.

- This document may contain tone-on-tone or color graphs, charts and/or pictures, which have been reproduced in black and white.

- This document is paginated as submitted by the original source.

- Portions of this document are not fully legible due to the historical nature of some of the material. However, it is the best reproduction available from the original submission.

NASA

Technical Memorandum 84938

The Flux and Source of Energetic Protons in Saturn's Inner Magnetosphere

A. W. Schardt and F. B. McDonald

DECEMBER 1982

National Aeronautics and Space Administration

Goddard Space Flight Center
Greenbelt, Maryland 20771

The Flux and Source of Energetic Protons in Saturn's Inner Magnetosphere

A.W. Schardt and F.B. McDonald
Laboratory for High Energy Astrophysics
NASA/Goddard Space Flight Center
Greenbelt, MD 20771

Abstract

The flux of energetic protons in Saturn's inner magnetosphere was observed in two channels from 48-63 and 63-160 MeV. Absorption features due to the G ring and the satellites Enceladus and Mimas were easily identifiable. The flux observed in the absorption slot of Mimas can be maintained by the decay of a cosmic ray albedo neutron flux of 7×10^{-3} cm^{-2} s^{-1} sr^{-1}. This flux is entirely consistent with calculations of the neutron flux produced by galactic cosmic ray interactions with the rings of Saturn. The omni-directional proton flux of 8.2×10^{3} cm^{-2} s^{-1} at 2.734 R_S requires a residence time of 30 years. Both the residence time and the energy spectrum are comparable to those found in the inner radiation belt of the Earth. The angular distribution is nearly isotropic in the Mimas slot and beyond $4R_S$. Otherwise the pitch angle distribution is pancake and has been approximated by $\sin^n\theta$ with n in the range 2-7. This distribution is consistent with an isotropic neutron source in the ring plane.

Introduction

Intense penetrating radiation was discovered by Pioneer 11 in Saturn's inner magnetosphere. This radiation was found between the orbit of Mimas (3.075 R_S) and the outer edge of the A ring (2.265 R_S). Protons with energies above 80 MeV are a major component of this radiation (Fillius et al., 1980; Fillius and McIlwain, 1980; Van Allen et al., 1980). Initially, we did not fully appreciate the sensitivity of the Goddard Space Flight Center/University of New Hampshire low energy detectors to the intense flux above 50 MeV (McDonald et al., 1980; Trainor et al., 1980) and attributed our Pioneer 11 observations to 1.1 - 8.1 MeV protons. Subsequent more detailed analysis of the response of these detectors showed that they could have responded to either low or high energy protons but that based on the observed flux above 50 MeV the contribution of high energy protons would be substantial inside the orbit of Mimas. A similar conclusion was reached by Simpson et al. (1981).

Mimas should stop the slow inward diffusion of protons, but McKibben and Simpson (1980) showed that the rapid episodic diffusion past Mimas during interplanetary disturbances was consistent with their initial interpretation of the data. Another explanation is based on the decay of energetic neutrons produced by cosmic ray interaction with Saturn's atmosphere and rings. This CRAND source is responsible for the high energy protons in the inner radiation belt of the Earth, and estimates indicated that a trapping lifetime of ~ 20 years would be required at Saturn to permit the flux to build up to the observed values (Fillius and McIlwain, 1980; Van Allen et al., 1980).

Voyager 2 carried two experiments identified as the Cosmic Ray Subsystem (CRS) and the Low Energy Charged Particle experiment (LECP), which observed the protons in the inner magnetosphere. Preliminary interpretation of the new data showed that any change in the high energy proton flux between 1979 and

1981 fell within the uncertainty of the measurements (Krimigis and Armstrong, 1982; Vogt et al., 1982). The LECP experiment also reported the proton spectrum and found a low energy component ($E < 0.5$ MeV) in addition to the high energy flux (Krimigis and Armstrong, 1982). The three-energy channel LECP measurement of the high energy proton flux peaks in the 54-87 MeV channel with lower fluxes near 10 MeV and 100 MeV. Good agreement was found in the absolute flux above 63 MeV between the CRS and LECP measurements.

The CRS on Voyager 2 was able to measure the proton flux in the inner magnetosphere in two channels (48-63 MeV and 63 - 160 MeV). The counter telescope used for this measurement had a low electron detection efficiency and was sensitive enough to collect adequate statistics in the important absorption slot produced by Mimas. This constitutes a major advantage over other experiments; however, the greater sensitivity also implied substantial dead-time and accidental coincidence corrections.

The Voyager 2 trajectory in the inner magnetosphere covered the latitude range from 30° to -20°. The latitude difference between the inbound and outbound passes permitted a measurement of the flux at two points on a field line, and intensity differences can be related by Liouville's theorem to the proton flux at two different equatorial pitch angles. These measurements do not permit an identification of the shape of the angular distribution; still they add to the Pioneer results which were either obtained with omni-directional detectors or shielded detectors whose angular response was uncertain because of shield penetration.

The purpose of this paper is to present a more careful analysis of our observations than was possible in the preliminary publication (Vogt et al., 1982) and to interpret the observed proton fluxes in terms of a balance between the proton source and the absorption due to the G and E-ring and the

satellites Enceladus and Mimas. We derive a new expression for satellite absorption for the case when the gyroradius of the particle is larger than the radius of the satellite and explore the effects of absorption by a satellite or dust ring on the energy spectrum of interacting protons. The analysis permits us to deduce the flux of CRAND neutrons required to maintain the observed proton flux. The strength of the neutron source is consistent with a source at the rings but too high for an atmospheric source. Our results do not find a natural explanation in terms of episodic diffusion.

Instrumentation

The CRS experiment has been described by Stone et al. (1977), and the data used in this paper were collected with the High Energy Telescope (HET). The high energy proton mode of the HET has three proton energy channels. Protons enter through detector B1 (Fig. 1), and a coincidence-anticoincidence matrix determines whether or not they stop in detector C4, C3, or C2. Alpha particles and heavy ions are discriminated against by an anticoincidence with a slant threshold. Electron sensitivity is minimized by high thresholds on detectors B2, C4, C3, and C2, which are well above the average energy deposited by an electron. Thus the higher order coincidences have very low electron sensitivity even though complete proton-electron separation is not possible in an individual detector.

The primary function of the HET is to monitor cosmic rays; consequently, the electronic circuits were designed with long time constants for good stability and low power consumption. At high rates, the anticoincidence circuits block only a fraction of the pulses and accidential coincidences become a problem. In order to operate in Saturn's inner magnetosphere, we turned off the low threshold detectors B1, C1, and the guard counters (Fig. 1,

Table 1). This offers two advantages: first, the efficiency of the anticoincidence shield becomes irrelevant and secondly, the solid angle for true coincidences is increased from 0.96 cm^2sr to 10.5 cm^2sr for B2, C4, C3. and C2 coincidences. Because the accidential coincidence rate remains unchanged, the true- to accidential-coincidence ratio becomes much more favorable. With this change the solid angles and proton energy ranges are less well defined and corrections are required for particles entering or escaping through the sides of the telescope. In addition, most alpha particles are now counted in the proton channels. They can no longer trigger the slant threshold because the B1 contribution to the summed pulse heights is absent. The sensitivity to alphas should present no problem in the inner magnetosphere where protons dominate the energetic particle population (McDonald et al., 1980; Simpson et al., 1980), but does change the cosmic ray response.

Corrections to the raw data were performed in two steps. The true coincidence rates were determined by correcting for accidental coincidences and losses due to the dead time of the electronic circuits. In the second step, we calculated the flux in specific energy ranges by taking account of the geometric factor and correcting for higher energy protons going through the sides. These corrections depend on the shape of the proton spectrum and were carried out reiteratively for power law and exponential spectra until neither the spectral index nor the flux changed. Errors in the final results were calculated by introducing appropriate uncertainties into the different corrections and adding all errors in quadrature. The flux in the 27-48 MeV range can, in principle, be derived from the B2, C4, $\overline{C3}$ rate; however, the corrections for higher energy particles passing through the side were so large that no reliable flux could be obtained in this energy range. A further

description of the logics and how the corrections were calculated is given in the Appendix.

Observations

The corrected coincidences rates are shown in Fig. 2, where R_2 represents the B2, C4, and C3 coincidence rate with C2 in anticoincidence and R_3 represents the B2, C4, C3, and C2 coincidence rate. Since the two rates are almost equal, the R_2 rate has been shifted down by 1 decade. Both the R_2 and R_3 rates were nearly constant from 10 to 5 R_S. They increased by three orders of magnitude and reached their maximum shortly after periapsis when Voyager was near the magnetic equator. Strong absorption features are seen at the orbits of Enceladus and Mimas. During the inbound pass, a spacecraft slew was performed near the G ring and produced a dip in the counting rates when the detector was pointed parallel to the magnetic field direction. The absorption of the G-ring at a constant pitch angle was observed during the outbound pass and produced only a change in the slope of the proton intensities.

The HET detector was reconfigured to the special operating mode at 10 R_S. Between there and 5 R_S, the observed coincidence counts were primarily due to cosmic ray protons and alpha particles. This deep penetration would not be expected on the basis of the Störmer cut-off rigidity (Table 2); however, both Pioneer 11 and Voyager 1 observed that the actual cut off of low energy protons (2-10 MeV) occurs between 7.5 and 10 R_S (McDonald et al., 1980; Vogt et al., 1981). It is believed that these low-rigidity particles gain access to the magnetosphere via the magnetotail. The presence of alpha particles can be deduced from the summed pulse heights of the C2, C3, C4 detectors because an appreciable fraction of the events has pulse heights in

excess of the total energy that can be deposited by a proton. Thus the trapping boundary for > 48 MeV protons may not be too far beyond 5 R_S.

The intensity increase starting inside the orbit of Tethys can be attributed to energetic protons. A more detailed examination is required to identify the source of the counts observed in the Mimas absorption feature between 3.02 and 3.14 R_S. A careful examination of our corrections showed that these counts cannot be due to accidental coincidences. The minimum dipole cut-off rigidities in this region are so high (Table 2) that even a somewhat reduced cut-off due to magnetotail access would filter out the large majority of the cosmic rays. The R_2 and R_3 counting rates are about the same at 3.08 R_S as between 5 and 6 R_S; therefore, residual cosmic rays can account for only a small fraction of the observed rates. We are either observing true proton coincidences or a residual electron sensitivity. Whether or not electron coincidences are present can be determined on the basis of the ratio between the singles rate in detector C3 and the particle flux derived from the coincidence rates. The geometry is such (Fig. 1) that detector C3 is shielded relatively uniformly with a threshold of approximately 48 MeV. If the coincidence counts are due to protons, then the flux above 48 MeV derived from the coincidence rates should be approximately equal to the C3 rate divided by its omni-directional geometric factor of 56.6 cm^2sr. This was true within ± 30 percent in the Mimas gap as well as at other places where we were clearly observing trapped protons. In contrast, if the coincidences were due to electrons, then the C3 rate should give a flux ~ 20 times larger than the coincidence rate because the low detection efficienty for electrons in detectors B2, C4, and C2 would give a much lower coincidence rate for equal electron and proton fluxes. This demonstrates that the coincidences are indeed due to a residual proton flux in the Mimas gap. Our data are

consistent with no electrons reaching C3; however, we cannot rule out the possibility that ~ 1/3 of the singles counts in C3 are due to electrons.

Fig. 3 gives the proton fluxes between 48-63 MeV and 63-160 MeV corresponding to the rates shown in Fig. 2. The flux was derived from the corrected rates by dividing by the geometric factor and correcting for particles going through the sides (see the appendix). The corrections in the 48-63 MeV channel were much larger than for the higher energy channel and depended on the slope of the spectrum. The flux in the two channels and the slope were calculated reiteratively. The values shown in Fig. 3 were calculated for an exponential energy spectrum ($j \propto \exp - E/E_{CH}$), but essentially the same values were obtained for a power law spectrum ($j \propto E^{-\gamma}$). Except during the spacecraft slew near the G-ring, the telescope pointed almost perpendicularly to the local magnetic field (Fig. 4). Near the Mimas absorption region, the 48-63 MeV flux could not be recovered because after correction the errors were comparable to the flux. The error bars in the inner magnetosphere are not due to counting statistics but reflect the uncertainties of the various corrections; thus, the curves are smooth in spite of the large error bars.

The spectral indices derived from the fluxes of Fig. 3 are shown in Fig. 5. No change in either E_{CH} or γ is noticeable at the orbit of Tethys; however, a distinct softening may be noticed near the orbit of Enceladus. We have no data on the spectral parameters in the Mimas absorption gap. The spectrum hardens at the G-ring (2.8 R_S) and appears to soften again at 2.734 R_S. Although the absolute errors are large near periapsis, relative values should be significant. The value of E_{CH} ~ 40 MeV observed at 2.734 R_S is similar to spectra found in the earth's radiation belt at L ~ 2.1 (Lavine and Vette, 1970).

In the inner magnetosphere identical fluxes at equal distances were observed between the inbound and outbound passes by Pioneer 11 but not by Voyager 2 (Figs. 2 and 3). The difference is that Pioneer stayed very near the equator while the latitude of Voyager 2 changed from +30° inbound to -20° outbound. The flux ratio at equal Equatorial distances between the two Voyager 2 passes provides information about the pitch-angle distribution. The calculated Equatorial distances depend critically on the magnetic field model used. As shown by Vogt et al. (1981, 1982), a centered dipole model is inadequate because the satellite absorption features are off-set relative to the position of the satellite. In this analysis we used the "Z3" model (Connerney et al., 1982) to obtain the field strength and Equatorial crossing of magnetic field lines going through the spacecraft. Tables of this model were kindly made available by Drs. Ness, Acuña, and Connerney. As can be seen from Figs. 2, 3 and 7, this model places the absorption features at the expected positions.

The experiment measured the integral flux $J(R, \theta_L)$ at a local pitch angle θ_L and field strength B_L. The local field and pitch angle are related by magnetic moment conservation (Schulz and Lanzerotti, 1974) to the Equatorial pitch angle θ and field strength B by:

$$\sin^2\theta = (B/B_L)\sin^2\theta_L \qquad (1)$$

Equatorial pitch angles corresponding to θ_L are shown in Fig. 4. According to Liouville's theorem, the local and Equatorial flux are the same at related pitch angles. We approximated the angular distribution by $\sin^n\theta$ to obtain the Equatorial flux at $\theta = 90°$ as a function of the local flux.

$$\mathcal{J}(R, 90^0) = \frac{J(R, \theta_L)}{[(B/B_L) \sin^2\theta_L]^{n/2}} \qquad (2)$$

where $\mathcal{J}(R, \theta)$ is the Equatorial flux and R is the radius at which the field line crosses the Equator.

The use of $\sin^n\theta$ for the angular distribution is an ad hoc assumption. The non-gyrotropic or first order anisotropy, which is not included in this expression, should be negligible because it depends on the ratio of the corotation velocity to the particle velocity and on the relative change of the flux over a distance of two gyroradii. Both of these effects are small except possibly for a gradient effect at the edges of the Mimas gap. A better approximation to the pancake pitch-angle distributions in the inner magnetosphere would be "a + $\sin^n\theta$" for θ in the range of 0 to 180°; this avoids the singularity at small pitch angles. Because we can derive only one parameter, we set "a" equal to zero to obtain a lower limit on the value of "n". The $\sin^n\theta$ angular distribution is not expected to hold in satellite absorption regions because particles are absorbed preferentially near 90° and a $\cos\theta \cdot \sin^n\theta$ distribution would be more appropriate. A negative value for n indicates that this is happening.

The value of n can be calculated from the intensity ratio between the inbound and outbound passes and is given by:

$$n = \frac{\log (J_{in}/J_{out})}{\log (\sin \theta_{in}/\sin \theta_{out})} \qquad (3)$$

where θ_{in} and θ_{out} are the Equatorial pitch angles. It should be noted that the effective angular resolution of the detector is improved because a given

The result shown in Fig. 6 does not represent an actual angular distribution but does indicate how the distribution changes with distance. The measurements are consistent with an isotropic distribution outside of 4 R_S, but the observations are relatively insensitive because they were made for equatorial pitch angles below 45°. Inside of 4 R_S, n increased rapidly to a value of ~ 7 at 3.26 R_S. This is the most anisotropic distribution we observed and occurs near the inner edge of the E-ring (Baum et al., 1981). The large anisotropy indicates that ring absorption must have been small in that region and is consistent with the inability of Voyager 1 to image the E ring inside of 3.5 R_S (Smith et al. 1981).

On either side of the Mimas gap, angular distributions may be approximated by $\sin^4\theta$. In the absorption gap, our measurements indicate a dumbbell distribution, but an isotropic distribution still falls within our errors. The spacecraft slew at ~ 2.8 R_S gives an independent observation of the pitch angle distribution of the proton flux in the G ring which can be represented by $0.4 + \sin\theta$. The actual angular distribution must be more anisotropic because of the loss of resolution by the ~ 70° acceptance cone of our detector. Inside the G ring, the distributions become more pancake again, but the closeness to the equator and large acceptance cone of the detector preclude meaningful measurements. In this region, Van Allen et al. (1980) found a $\sin^4\theta$ distribution and Krimigis and Armstrong (1982) reported $\sin^5\theta$.

A phase space density analysis was performed to identify the proton source region and to determine the direction of diffusive flow from the slope of the density. For non-relativistic particles, the Vlasov distribution function in momentum space is related to the differential flux j by $f = j/(2m\,E)$, where m is the proton mass and E its energy. Because our measurements give only the integral flux, J, between lower, E_1, and upper, E_2, energy thresholds, we

have to use the shape of the spectrum to calculate the distribution function. We also extrapolated our measurements to an equatorial pitch angle of 90° in order to follow the change in density of protons that mirror near the equator. The following expressions were used:

$$f(E, R, 90^0) \propto \frac{J(R, \theta_L)}{[(B/B_L) \sin^2\theta_L]^{n/2}} g(E) \qquad (4)$$

$$g(E) = \frac{(\gamma-1)\ E^{-(\gamma+1)}}{E_1^{-(\gamma-1)} - E_2^{-(\gamma-1)}} \qquad (5a)$$

$$g(E) = \frac{\exp - E/E_{CH}}{E\ E_{CH}[(\exp - E_1/E_{CH}) - (\exp - E_2/E_{CH})]} \qquad (5b)$$

where equ. (5a) applies for power law spectra ($j \propto E^{-\gamma}$) and eq. (5b) for exponential spectra ($j \propto \exp - E/E_{CH}$). Values of the spectral index γ or characteristic energy E_{CH} are shown in Fig. 5.

We want to follow particles with a constant first invariant that is with a fixed magnetic moment as they diffuse inward; therefore, the distribution function for non-relativistic particles has to be calculated at energies related by:

$$E = \frac{E_o}{B_o} B(R) \qquad (6)$$

where E_o and B_o are the reference energy and magnetic field and B(R) gives the equatorial field at distance R. The magnetic moment was chosen such that the proton energy fell primarily into the 48-160 MeV range. This restricted the analysis to 15 BeV/G particles inside the orbit of Enceladus and 60 BeV/G

between 6 and 4 R_S. Fig. 7 shows the results for an exponential spectrum and characteristic energies of 40 MeV for the 15 BeV/G curve and 33 MeV for the 60 BeV/G curve.

As can be seen from equ. (4), the value of the distribution function depends on the angular distribution through the parameter n of the $\sin^n\theta$ distribution. In order to demonstrate that the angular distribution changes with distances, we plotted the relative phase space densities based on a $\sin^2\theta$ distribution in Fig. 7a; Fig. 7b shows relative phase space densities for the angular distribution parameters shown in Fig. 6. A comparison between Figs. 7a and 7b shows that the major trend versus distance of the distribution function is not changed by specific assumptions about the angular distribution.

Relative phase space densities calculated with power law spectra are very similar to those shown in Fig. 7. A minor difference occurs between 4.2 and 5 R_S for 60 BeV/G protons; the power law spectrum with $\gamma = 2.2$ gives a noticeable minimum at 4.7-4.9 R_S. The density ratio between 3.3 and 4.3 R_S for 15 BeV/G protons is 30 for $E_{CH} = 40$ MeV but only 11 for $\gamma = 1.5$. Such differences are to be expected because the radial dependence of the distribution function is sensitive to the slope of the energy spectrum. For the purpose of this paper, however, these inaccuracies are not important because they do not alter the conclusions to be discussed later.

The slope of the distribution function shown in Fig. 7b vanishes at 2.8 - 2.90, 3.33, and in a broad region between 4.5 and 5 R_S. A slight dip or at least a flat region occurs at ~ 2.8 R_S, where both the first and second derivatives vanish. On this basis, the diffusive flow of protons between 3.33 and 4.5 R_S is towards Enceladus from both sides, and the flow between 2.90 and

3.33 is towards Mimas. Protons from inside 2.8 R_S diffuse on the average out towards the G-ring, but the the diffusive flow vanishes in the G ring.

Proton Absorption by Moons and Dust Rings

The absorption of trapped particles has been treated by several authors. We follow the approach of Mead and Hess (1973) and Thomsen et al. (1977). A characteristic lifetime against absorption is calculated by averaging over gyroperiod, bounce period, drift period and the range of radial distances between the absorber and the gyrocenter of the particle. The geometric absorption cross section is used for the satellite. This approach does not pick up minor resonances such as between drift period and bounce period; however, these resonances are in general too narrow to contribute significantly to the lifetime. Previous work was primarily applicable to lower energy particles. The effective absorption cross section of the satellite for these particles is that of a sphere with a radius equal to the satellite radius plus the gyroradius of the particle. All particles are absorbed if the motion of the gyrocenter intercepts the sphere. This simple model underestimates the characteristic lifetime of high energy particles if they are absorbed by a small satellite like Enceladus or Mimas. Since our initial writing of this paper, we have become aware of an internal University of Iowa report (Rairden, 1980) which treats this problem numerically. Their discussions and numerical simulation support the analytical treatment given below.

Let us first calculate the characteristic lifetime of protons which are injected uniformly over the sweeping region of a satellite. This is the case for a CRAND source and the eccentric orbit of Mimas. Protons drift relative to the satellite with a period τ_d, and the fraction P is absorbed each time they

drift past the satellite. An average value of P is required because P is a function of the distance between the satellite and the path of the gyrocenter. If j is the differential proton flux at energy E, then $\langle P \rangle \cdot j$ is the decrease in flux per drift period. For a stable proton population, we need a source S_p of such strength that:

$$S_p \tau_d = \langle P \rangle \cdot j \tag{7}$$

If the proton flux is given in units of $cm^{-2}\ s^{-1}\ sr^{-1}$, the S_p is in units of $cm^{-2}\ s^{-2}\ sr^{-1}$. This permits us to define a characteristic proton lifetime against absorption

$$\tau_p = \frac{\tau_d}{\langle P \rangle} \tag{8}$$

such that it gives $S_p = j/\tau_p$. In the following, we use the equations of Thomsen and Van Allen (1980) to describe the particle motion but use the equatorial magnetic field at Mimas of 0.007338 gauss given by the Z3 model. The equation for the particle bounce period τ_b contains the integral $H(\theta)$ along the field line, and as Birmingham (1982) has shown, the dipole value of this integral is still applicable at 3 R_S.

Most of the symbols to be used are defined in Table 3. The lifetime of a proton population on a specific drift shell depends on the probability that protons can drift past the satellite without being absorbed. This can happen because a) a proton may be near a mirror point and does not cross the equator as it drifts past the satellite; b) even though it crosses the equator it may be in the wrong gyrophase to hit the satellite; and c) for an eccentric

satellite orbit, the satellite may be temporarily too far away from the drift shell to be intercepted.

Each particle crosses the equator twice during a bounce period; therefore, $2t_a/\tau_b$ gives the fraction of the particles that cross the equator during the time t_a to be derived shortly when their trajectory intercepts the satellite. If the gyroperiod $\tau_g \leq t_a$, a particle with a 90° pitch angle cannot drift past the satellite without being lost; however, if $\theta \neq 90°$, it may skip the satellite vertically provided it moves more than the satellite's diameter in one gyroperiod (Fig. 8c). For a particle velocity V, the vertical distance is given by $V_{\parallel}\tau_g$, and the fraction lost is $2r/V_{\parallel}\tau_g$, provided that $r/(\pi\rho) << 1$. As McDonald et al. (1980) have shown, vertical skipping reduces absorption probabilities considerably for > 2 MeV protons at Mimas. In an eliptic orbit, a satellite spends a larger fraction of its time at either extreme than near the middle of the absorption region; however, for the purpose of this calculation we have assumed equal probability for any distance between the maximum and minimum radius of the orbit. In that case $2(\rho + r)/\Delta R$ gives the probability that the gyrocenter is close enough for absorption. Combining the three factors, we find the probability that the particle is absorbed as its gyrocenter drifts past the satellite:

$$P = \left(\frac{2t_a}{\tau_b}\right)\left(\frac{2r}{V\,\tau_g\cos\theta}\right)\left(\frac{2(\rho + r)}{\Delta R}\right) \qquad (9)$$

In equation 9, $V_{\parallel}$ has been replaced by V cosθ. It should be noted that the absorption probability due to any one of the three factors discussed above cannot exceed unity, and expressions given in the three brackets of equ. 9 become incorrect when this happens. In particular, the second factor should

be set equal to 1 for $\cos\theta < 2r/(V\tau_g)$, that is near 90°; the third factor is 1 at Enceladus where $\Delta R < 2(\rho + r)$.

The period of time during which particle trajectories intercept the satellite can be calculated from the encounter geometry. As shown in Fig. 8, the gyrocenter has to be located somewhere in the interval of length D if the leading side of the gyrocircle is to intercept the satellite. An equal distance is available for an intercept by the lagging side. If v_d is the drift velocity, then t_a is given by

$$t_a = \frac{2D}{v_d} = \frac{D\,\tau_d}{\pi\,R} \tag{10}$$

v_d has been expressed in terms of τ_d in the second part of Equ. 10. D is given by the following expressions (Figure 8a, b):

$$D = \sqrt{(\rho + r)^2 - x^2} - \sqrt{(\rho - r)^2 - x^2} \quad \text{for} \quad x < (\rho - r) \tag{11}$$

$$= \sqrt{(\rho + r)^2 - x^2} \qquad \text{for} \qquad (\rho - r) < x < (\rho + r)$$

where x stands for the distance between the center of the satellite and the drift path. The average value of D with equal weight for each x is

$$\langle D\rangle = \left[\int_0^{\rho + r} D\,dx\right] / \int_0^{\rho + r} dx$$

$$\langle D\rangle = \frac{\pi\,\rho\,r}{\rho + r} \qquad \text{for } \rho > r \tag{12}$$

$$= \frac{\pi}{4}(\rho + r) \qquad \text{for } r > \rho$$

and

$$\langle t_a \rangle = \frac{\rho \, \tau_d}{R \, (\rho + r)} \quad \text{for } \rho > r \tag{13}$$

If we substitute Equation (13) for $\langle t_a \rangle$ and $\tau_b = 4R\ H(\theta)/V$ in Equation (9), we find the average absorption probability per drift period:

$$\langle P \rangle = \frac{2\ \rho_o r^2\ \tau_d\ \sin\theta}{R^2\ \Delta R\ \tau_g\ H(\theta)\ \cos\theta} \tag{14}$$

$H(\theta)$ is the line integral between mirror points, defined in Equation 14 of Thomsen and Van Allen (1980) and assumes values between 0.74 at $\theta = 90°$ and 1.38 at $\theta = 0°$; ρ_o is the gyroradius for $\theta = 90°$.

From Equation (8), (14), $\tau_g/\rho_o = 2\pi/V$ and the relation between particle velocity and energy, we find the characteristic lifetime at equatorial pitch angle θ:

$$\tau_p = \frac{\pi R^2\ \Delta R\ H(\theta)}{V\ r^2\ \tan\theta} = \frac{\pi R^2\ \Delta R\ H(\theta)}{c\ r^2\ \tan\theta} \cdot \frac{E + E_o}{\sqrt{E(E + 2E_o)}} \tag{15}$$

$$\text{for } \theta \neq 90^0 \text{ or } 0^0$$

$$\tau_p = 6.988 \times 10^4\ \frac{H(\theta)}{\tan\theta}\ \frac{E + 938.21}{\sqrt{E(E + 1876.42)}} \quad \text{for protons at Mimas}$$

The particle energy E and rest mass E_o are in MeV, c is the velocity of light, and τ_p is in seconds. Equation 15 does not hold at 90° where it underestimates τ_p, nor near 0° ($\rho_o \sin\theta < r$) where it overestimates τ_p. However, we can find the lifetime averaged over pitch angle $\langle \tau_p \rangle_\theta$ from Equation 15 if the solid angle subtended by these regions is small. For an isotropic pitch angle distribution, this gives at Mimas:

$$\langle \tau_p \rangle_\theta = 6.99 \times 10^4 \frac{E + 938.21}{\sqrt{E(E + 1876.42)}} \qquad (16a)$$

Equ. 15 and 16a give relativistic expressions; however, we will use primarily the non-relativistic approximation in our energy range E << 938 MeV. In contrast to the lower energy expressions (Thomsen et al., 1977), τ_p is independent of the drift period, depends sensitively on the equatorial pitch angle, and has a weak energy dependence, proportional to $E^{-1/2}$ for non-relativistic particles.

The above expressions apply to differential energy spectra. To handle an integral flux, we have to average equ. 15 over energy to find $\langle \tau_p \rangle_E$ or alternately find the effective energy at which τ_p is equal to the average value. If J is the integral flux between energies E_1 and E_2, then

$$J = \int_{E_1}^{E_2} \tau_p S_p dE = \langle \tau_p \rangle_E \int_{E_1}^{E_2} S_p dE \qquad (16b)$$

Now we can make use of the non-relativistic approximation to equ. 15 to calculate the effective energy E_{eff} which is given by:

$$E_{eff} = \left[\int_{E_1}^{E_2} S_p dE \; / \int_{E_1}^{E_2} E^{-1/2} S_p dE \right]^2 \qquad (16c)$$

For this calculation we approximated the source spectrum by the proton spectrum at 2.73 R_S which is of the forum $S_p \propto \exp -E/E_{CH}$. For the range 63-160 MeV, E_{eff} is equal to 90 MeV if $E_{CH} \sim 40$ MeV; E_{eff} does not depend sensitively on the value of E_{CH}. In addition, τ_p does not vary rapidly with energy; thus, these approximations have only a secondary effect on $\langle \tau_p \rangle_E$.

The approach used for uniformly injected protons has to be modified for protons diffusing into the Mimas absorption region because the gyrocenters are

not uniformly distributed over x but start out at the edges of the absorption region. If diffusion is slow, protons are absorbed only every 22 h 37 m when Mimas is near the edge. Most of the absorption should occur where the absorption probability is highest, that is at $x = \rho - r$ where

$$D = 2\sqrt{\rho r} \tag{17}$$

Using this value for D, we can calculate the absorption lifetime while Mimas is at the extremes of its orbit. In that case, only the first and second factors in equ. 9 are relevant:

$$\tau = \frac{\pi R^2 \tau_g H(\theta) \cos\theta}{2r\,(\rho_0 r \sin\theta)^{1/2}} \tag{18}$$

$$\tau = 8.801 \times 10^2 \frac{E + 938.21}{[E(E + 1876.42)]^{1/4}} \frac{H(\theta)\cos\theta}{\sqrt{\sin\theta}} \quad \text{for protons at Mimas (E in MeV)}$$

This lifetime is given as the last entry in Table 3. The 48 min lifetime of 90 MeV protons at $\theta = 85°$ shows that near equatorial protons are indeed lost each time around because Mimas spends each period ~ 3 h near apoapsis and near periapsis. The distance most of these protons can diffuse in one period of Mimas is expected to be small compared to the width of the gap; thus, these protons cannot penetrate into the gap. In contrast, at $\theta = 45°$ the proton lifetime is 8.8 hrs and about 70 percent survive each encounter; therefore, they can penetrate some distance. Thus their lifetime may actually be closer to the lifetime of randomly injected protons. These conclusions are consistent with our data. Although the counting statistics are marginal,

there is a distinct indication (Fig. 2 and 3) of a square Mimas absorption slot for $\theta = 75°$ (outbound) and a rounded slot for $\theta = 45°$ (inbound).

The characteristic lifetime at Enceladus is also given by equ. 18. The orbital eccentricity of Enceladus is small, and the third factor of equ. 9 is unity when $\Delta R < 2(\rho + r)$. Because the width of the sweeping region is less than a gyroradius, most of the protons are diffusing towards Enceladus, rather than being injected into the gap; thus, equ. 17 gives the appropriate value for D. The energy dependence of τ is proportional to $E^{-1/4}$. Consequently, absorption by Enceladus will produce a somewhat softer spectrum than the injection spectrum.

Absorption by a dust ring affects the trapped particle population quite differently from satellite absorption if the dust particles are small compared to the range of the protons (less than a fraction of a mm in our energy range). Strong forward scattering of light by both the E and G rings (Smith et al., 1982) suggests that these rings are largely made up of μm-sized particles. Under these circumstances, the ring absorption resembles energy loss in the upper atmosphere treated by Hess (1968), but the pitch angle dependence is quite different because atmospheric absorption occurs primarily near the mirror point and increases rapidly as the mirror altitude decreases. In contrast, at Saturn protons lose an energy ΔE each time they pass through the ring:

$$\Delta E = \frac{w}{\cos\theta} \frac{dE}{dx} \tag{19}$$

where w is the mass per unit area of the ring (gm cm^{-2}), and dE/dx is the stopping power (MeV cm^2 gm^{-1}). This gives an average rate at which particles lose energy of $(-dE/dt) = 2\Delta E/\tau_b$. If N(E)dE is the number of particles per

cm^3 in the interval dE, then N(E) • (dE/dt) gives the flow of particles in energy, and the number lost is given by the gradient. For a stable population, a source is required to cancel the loss (equ. 4.2 in Hess, 1968):

$$\frac{d}{dE}\left[N(E)\,\frac{dE}{dt}\right] = S_p' \qquad (20)$$

where S_p' is the source of particles. Solve equ. 20 and substitute the above expression for dE/dt, j/V for N(E) and S_p/V for S_p', where V is the proton velocity and S_p is the proton flux injected per second in units of cm^{-2} s^{-2} sr^{-1} MeV^{-1}. The resulting expression for the differential proton spectrum is:

$$j = \frac{\tau_b \sqrt{E}\,\cos\theta}{2w\,(dE/dX)} \int_E^\infty \frac{S_p}{\sqrt{E'}}\,dE' \qquad (21)$$

If we are primarily interested in the change of the energy spectrum due to absorption, then the energy dependence can be approximated by a power law: $S_p \propto E^{-\gamma}$, $\tau_b \propto E^{-1/2}$ and $dE/dx \propto E^{-0.75}$. The value of 0.75 was calculated from the stopping power of silicon in the 10-160 MeV range and is not much different for lighter elements in the rings. Substituting these values in equ. 21, we find

$$j \propto E^{-(\gamma-1.25)} \qquad (22).$$

The exponent γ-1.25 shows that the proton spectrum should be significantly harder than the injection spectrum and could turn over if $\gamma < 1.25$. This is in contrast to absorption by satellites where the proton spectrum should be softer than the local source.

Discussion

The CRS observations measured the proton flux (Fig. 3) in two channels (48-63 and 63-100 MeV). Based on this data, we have determined the slope of the energy spectrum (Fig. 5) and obtained a general idea of changes in the angular distribution with distance (Fig. 6). Our analysis of the data demonstrated a substantial inward increase in the phase space density of 15 BeV/G protons (Fig. 7) and thus confirmed the interpretation of Pioneer 11 data by Van Allen et al. (1980). The most significant new result is the measurement of the energetic proton flux (63-160 MeV) in the Mimas absorption region. Because we can calculate the characteristic lifetime against absorption by Mimas, this measurement permits us to deduce the strength of the proton source required to maintain the observed flux. Based on the strength of the proton source, we can establish the strength of the CRAND neutron source.

The particle distribution function in momemtum space obeys, on the time scale of interest to us, the steady-state diffusion equation (Schulz and Lanzerotti, 1974):

$$\frac{\partial f}{\partial t} = L^2 \frac{\partial}{\partial L} \left(\frac{D}{L^2} \frac{\partial f}{\partial L}\right) + S_p - \ell_p = 0 \qquad (23)$$

where D is the diffusion coefficient, S_p the local proton source and ℓ_p the loss term. Over the small range of L under consideration, we can consider D and D/L^2 as constant and write equ. 23 as:

$$D \frac{\partial^2 f}{\partial L^2} + S_p - \ell_p = 0 \qquad (23a)$$

If τ_p is the characteristic lifetime then ℓ_p is given by:

$$\ell_p = \frac{f}{\tau_p} \qquad (24)$$

Within statistical errors the distribution function is flat in the Mimas gap (Fig. 7); thus its second derivative vanishes or is at most small. Therefore by equ. 23a, the local loss and source terms balance in the gap. This intepretation is consistent with the discussion in the last section in which we showed that protons with pitch angles near 90° should be absorbed near the edge of the gap and that the flux in the gap has, therefore, to be replenished by a local source. In view of the non-relativistic relation between the proton flux and distribution function, $f = j/(2mE)$, and the short range in L, we can substitute the proton flux for the distribution function in equ. 23a and 24 to obtain $S_p = j/\tau_p$ where S_p was defined in equ. 7 and is equal to $2mE\ \Sigma_p$. The required neutron flux is related to the proton source strength by (Cooper and Simpson, 1980; Blake et al., 1983):

$$j_n = \frac{\tau_n}{\chi} S_p = \frac{\tau_n}{\chi\ \tau_p} j \qquad (25)$$

where $\tau_n = 10^3$ sec is the neutron decay halflife, χ the proton injection efficiency, and j_n the CRAND neutron flux.

To calculate the integral proton source and neutron flux in the interval 63-160 MeV, we calculated the effective energy with equ. 16c and used the value of E_{eff} to calculate τ_p with equ. 15 (Table 3). Indications are that another small satellite or absorbing material exists in this region in addition to Mimas (Simpson et al., 1980; Vogt et al., 1982), but this object is too faint to have shown up in Voyager images (Synott et al., 1981; Smith et al., 1982). Therefore we feel justified in using τ_p for Mimas because τ_p is proportional to r^{-2} and such a small object should not decrease τ_p signifi-

cantly. Values of χ at L = 3.075 were obtained by interpolating between graphs of χ vs. pitch angle calculated by Blake et al. (1983) for an isotropic neutron source. We measured a proton flux of 6×10^{-2} cm^{-2} s^{-1} sr^{-1} at a 45° Equatorial pitch angle inbound and 4×10^{-2} cm^{-2} s^{-1} sr^{-1} at 75° outbound. These and the other pertinent parameters are listed in Table 4. Based on these results, our best value for the neutron flux is 7×10^{-3} cm^{-2} s^{-1} sr^{-1}. This value has been increased by 10%, as compared to the average of the two measurements in Table 4, in order to correct for protons above 160 MeV which were not counted.

We have made a plausible argument that the source and loss terms in equ. 23a should balance locally at the center of the Mimas gap; however, our counting statistics are too poor to prove rigorously that $\partial^2 f/dL^2 = 0$. Should this not be the case, we have overestimated the required source strength. A lower limit for the source strength can be established by assuming that protons diffusing into the gap are uniformly distributed in the gap and that diffusion is loss free except in the Mimas absorption region. We integrate equ. 23a between 2.90 and 3.33 R_S. Because the first derivative of the distribution function vanishes at both endpoints, we have:

$$\int_{L_1}^{L_2} \tilde{S}_p \, dL > \int_{\text{Mimas}} f/\tau_p \, dL \qquad (26)$$

Over the small range in L, the proton source strength is approximately constant, and we obtain the following lower limit:

$$S_p > \frac{\Delta L}{L_2 - L_1} \frac{j}{\tau_p} = \frac{j}{3.5\tau_p} \qquad (27)$$

This proves that the required source strength can be no lower than 30 percent of the value derived above (equ. 25).

The experimental value of 7×10^{-3} cm^{-2} s^{-1} sr^{-1} for the neutron flux is consistent with calculations of the expected CRAND flux from Saturn's rings (Table 4). Cooper and Simpson (1980) estimated a neutron flux of $\sim 10^{-2}$ cm^{-2} s^{-1} sr^{-1}. Blake et al., (1983) obtained a value of 8×10^{-5} cm^{-2} s^{-2} for the source strength of protons above 10 MeV at 2.65 R_S and $\theta = 65°$. Their value can be extrapolated to the orbit of Mimas by using the ratio of the injection efficiencies at the two distances. In terms of source strength per unit solid angle, the extrapolated value is 4×10^{-6} cm^{-2} s^{-2} sr^{-1} as compared to our value of 9×10^{-7} cm^{-2} s^{-2} sr^{-1}. Our value is significantly lower, but their figure also includes protons between 10 and 63 MeV. Saturn's atmosphere provides only a minor fraction of the CRAND neutrons because its flux is only $< 10^{-4}$ cm^{-2} s^{-1} sr^{-1} (Cooper and Simpson, 1980), or more than 2 orders of magnitude below the required flux.

Confirmation that the protons are produced by albedo neutron decay is offered by the proton spectrum and angular distribution. The slope of the spectrum above 48 MeV observed at 2.74 R_S resembles the CRAND proton spectrum at earth near L = 2.1 (Levine and Vette, 1970) and falls within the range of spectra predicted for a source at Saturn's rings (Blake et al., 1983). A pancake distribution is also consistent with a neutron source at the ring plane provided the neutrons can escape isotropically. For this case, Blake et al. (1983) predict an angular distribution of approximately $\sin^5\theta$, which is close to our observations outside the absorption regions, that is between 3.5 R_S and the orbit of Mimas and outside the G-ring to the orbit of Mimas (Fig. 6).

Once the source strength is known, we can calculate the proton residence time in different parts of the inner magnetosphere. In a loss free diffusion

region this gives the time required to build up the observed flux, while it gives the lifetime against absorption in a region dominated by local losses. Table 5 lists both the omni-directional proton flux and the residence time which is given by the ratio between the flux and source strength ($\sim 8.8 \times 10^{-6}$ protons cm^{-2} s^{-2}). The omni-directional flux at periapsis, 2.734 R_S, is based on our measurement at a 55° pitch angle and $\sin^4\theta$ distribution; ± 20 percent covers distributions from $\sin\theta$ to $\sin^6\theta$. The residence time of 30 y is consistent with those found in the inner radiation belt of the earth. The residence time is 12 y in the G-ring; this is the lifetime against absorption because both the first and second derivatives of the distribution function vanish in this region (Fig. 7b). The residence time has decreased to 1.4 y at 3.33 R_S. Because the second derivative of the distribution function is negative, the local source is larger than the local loss term. We may conclude that diffusion away from 3.33 R_S plays a significant role in limiting the residence time.

We are now able to compare omni-directional fluxes observed by different instruments. At 2.734 R_S, Pioneer 11 measured fluxes of 1.5×10^4 cm^{-2} s^{-1} (Van Allen et al, 1980) and 1.1×10^4 cm^{-2} s^{-1} (Fillius et al, 1980) for the integral proton flux above 80 MeV. Using our energy spectrum (E_{CH} = 40 MeV) and the results given in Table 5, we obtain 5.9×10^3 cm^{-2} s^{-1} above 80 MeV which is about half as much as the Pioneer 11 result. Krimigis (private communication) measured a flux of 3.8×10^3 cm^{-2} s^{-1} of 16-160 MeV protons at the same distance but at a latitude of 8.2°; this translates to a flux of 4.5×10^3 cm^{-2} s^{-1} at the equator for a $\sin^5\theta$ distribution. This should be compared to our value of 8.2×10^3 above 63 MeV. As can be seen, the different observations are within a factor of 2 of our value, and the spread can be accounted for by the substantial differences between the instruments

and the difficulty of obtaining a true omni-directional flux in the presence of a very anisotropic pitch angle distribution. These observations are, therefore, consistent with the required residence time; however, they can not be used as proof of such stability.

Local losses modify the observed proton spectrum as compared to the injection spectrum. For losses due to absorption by dust rings or satellites, the direction of the change from the source spectrum can be deduced on the basis of the processes discussed in the previous section. The characteristic lifetime due to satellite absorption decreases with proton energy; therefore, spectra should be softer in the Mimas and Enceladus absorption regions. We were unable to measure spectral parameters at Mimas; however, a steepening of the spectrum was observed at Enceladus (Fig. 5).

Based on the model of dust-ring absorption, spectra should become harder in the G and E-ring. Specifically the index γ of a power law spectrum ($j \propto E^{-\gamma}$) should decrease by 1.? in the G-ring where local absorption dominates. Unfortunately, the errors on our measurement of γ in this region are large, but relative errors should be substantially smaller, and the trend (Fig. 5) between 2.734 and 2.82 R_S is in the expected direction. This effect may also be the reason for the inverse slope (negative γ) observed by Krimigis and Armstrong (1982) between 20 and 50 MeV. The neutron spectrum should be almost flat in this energy range (Blake et al., 1983), and the slope of the proton spectrum should reverse. Any E-ring absorption is superimposed on effects due to Enceladus. Changes in the spectrum above 48 MeV indicate that absorption by Enceladus dominates, while the 10-50 MeV data of Krimigis and Armstrong favor E-ring absorption. It is not yet clear how to reconcile these apparently contradictory results.

By now the reader may have become aware that we carefully avoided a discussion of the diffusion coefficient. Diffusion theory has been applied extensively to loss free diffusion and localized sources and sinks, but a more detailed analysis is required if extended source and loss terms are involved. Changes of the distribution function with radial distance have to be analyzed and the second derivative (equ. 23) is especially important. Such an analysis is planned to derive the proton diffusion coefficient and the density of the G ring.

Conclusions

The properties of the energetic proton flux (48-160 MeV) in the inner magnetosphere of Saturn are entirely consistent with a CRAND source at the rings. In particular, the residual flux in the sweeping region of Mimas is consistent with local injection from neutrons decaying in this region and requires a neutron flux of 7×10^{-3} cm^{-2} s^{-1} sr^{-1} above 63 MeV. This is consistent with the neutron flux expected from cosmic ray interaction with the rings (Blake et al., 1983; Cooper and Simpson, 1980). The angular distribution of the protons requires a nearly isotropic neutron source which suggests that the neutron absorption in the ring plane is relatively small. The proton trapping lifetime is comparable to that found in the earth's inner radiation belt.

We can also ask whether our results can be explained equally well by episodic diffusion as the mechanism which transports protons past the satellites to populate the inner magnetosphere (McKibben and Simpson, 1980). The phase space density increases about 30 times between 4.3 and 2.74 R_S. A large diffusion mean free path during disturbed conditions can explain diffusion past Mimas but does not result in an increase in phase space density

as long as the diffusion process is reversible. This requires that the proton density outside of Mimas at 4.3 R_S must have been 30 times the observed value when the episodic diffusion mechanism operated. This problem does not arise, and the phase space density can increase inward if inward displacements are always larger than outward steps (McKibben and Simpson, 1980). This would be the case if the mean free path is proportional to L^m with $m > 0$; however, such irreversibility in magnetospheric diffusion has not yet been demonstrated. The proton spectrum provides further evidence; it is consistent with CRAND injection and considerably harder than would be expected from the inward diffusion of the proton population found in the outer magnetosphere. The variable and highly anisotropic angular distribution, proportional to $\sin^n\theta$ with $n = 4\text{-}7$, would not be expected from inward diffusion. Any one of these points by itself could be consistent with episodic diffusion, but collectively they strongly favor a CRAND source.

Acknowledgements: The authors are indebted to the Voyager magnetometer team headed by N.F. Ness for permission to use their magnetic field data; R.P. Lepping was particularly helpful in preparing the data. Tables of the Z3 magnetic field model were made available by J.E. Connerney, M.H. Acuña and N.F. Ness. Discussions with T.J. Birmingham and helpful comments by J. Van Allen and M. Thomsen are gratefully acknowledged. This work benefitted greatly from the close collaboration and assistance given by the CRS team members and collaborators at the California Institute of Technology and D.L. Chenette at the Aerospace Corp. We also want to express our thanks to the Voyager Project Team for their support in carrying out this investigation.

Appendix

Corrections for Counter Dead Time, Accidental Coincidences, and Particles Penetrating Through the Sides

In the inner magnetosphere of Saturn the HET detector (Fig. 1) operated at much higher rates than normal, and extensive corrections were required to derive the true proton flux. These corrections depend on the time-constants and logics of the electronic system and on the new geometric configuration which was produced when detectors B1, C1, and the guard counters were deactivated. Three different corrections where required: (a) dead time correction for the counts lost, (b) subtraction of accidential coincidences to obtain true coincidence rates, and (c) corrections for higher energy particles that pass through the side of the detector. Because corrections to the B2 C4 $\overline{C3}$ rate were too large to obtain a valid flux between 27-48 MeV, we will discuss in the following only the B2 C4 C3 $\overline{C2}$ and B2 C4 C3 C2 coincidence rates.

The logic of the HET coincidence-anticoincidence matrix is controlled by a strobe pulse. After the strobe pulse is triggered by a particle entering the telescope, the discriminators on each detector of the telescope are interrogated to see whether or not they were fired. The event is added to that rate counter which corresponds to the observed combination of triggered detectors; if no match is found, the event is discarded. The individual counting rates of each detector are monitored in space. Extensive ground calibrations permits us to derive dead time losses and accidential coincidence corrections from these rates.

The dead time associated with each detector is controlled by the recovery time τ_d of the discriminator. If R is the true and N the observed rate of a detector, then

$$R = \frac{N}{1-\tau_d N} \qquad (A1)$$

where $1-\tau_d N$ is the fraction of time that the detector is sensitive. For HET $\tau_d \sim 16$ μs with some dependence on pulse amplitude. The pulse height dependence was not included in this analysis, and we estimate that the uncertainty in τ_d is ± 15%. Corrections calculated with equ. A1 were applied to coincidences involving the C2 and C3 detectors (Fig. 1). The combined dead time correction for the B2, C4, strobe (ST) coincidences was determined from large pulses which triggered the heavy ion slant threshold (SL). The trigger rate of SL was low enough that it required no correction. Most events cannot trigger SL without also triggering at least B2 and C4, and the ratio of the B2, C4, ST, SL rate to the SL rate gives the fraction of the large pulses which succeed in triggering B2, C4, ST coincidences. This ratio varied between 0.3 when B2 was 3×10^4 counts s^{-1} and ~ 0.95 for 10^3 counts s^{-1}. However, it is not only a function of the B2 rate but also of the counting rates of other detectors in HET. Therefore, we attributed a ± 30% uncertainty to this correction.

The calculation of accidental coincidences is simplified if we use the actual counting rates of the detectors rather than true rates because then the dead time insures that two counts cannot occur in rapid succession and be recorded as only one accidental count. Let τ_a be the length of time that the strobe pulse will record a coincidence after a detector is triggered . For a counting rate N, and a true coincidence rate N_t the fraction of the time that

accidental coincidences are possible is $\tau_a(N - N_t)$; during this time strobe pulses not associated with true coincidences will give accidental coincidences. Therefore

$$N_a = (ST - ST_t)\,\tau_a\,(N - N_t) \qquad (A2)$$

where N_a is the accidential coincidence rate, ST the total strobe rate that can be in coincidence with N, and ST_t represents the strobe pulses in true coincidence. In our circuits τ_a depends on N and falls in the range of 26μs at low rates to 15μs at ~ 1.5×10^4 counts s^{-1}. The accidental coincidence time was approximated by a quadratic in N and given a 15% uncertainty.

Let us use the following notation for counting rates in applying equ. A2 to HET: N_1 = B2 C4 $\overline{C3}$, N_2 = B2 C4 C3 $\overline{C2}$ and N_3 = B2 C4 C3 C2 coincidence-anticoincidence combinations (the line over the symbol of a detector denotes anticoincidence). Use subscripts "a" and "t" to denote accidental and true coincidences and use the symbol of the counter for its counting rate. Then the strobe rate which can be in accidental coincidence with detector C2 is $N_2 + N_3 - N_{3t}$. Therefore

$$N_{3a} = (N_2 + N_3 - N_{3t})\,\tau_a\,C2$$
$$N_3 = N_{3a} + N_{3t} \qquad (A3)$$

In the above expression we have ignored the small correction for true coincidences to the singles rate of detector C2. The equivalent expression giving the total accidental rate involving detector C3 is given by

$$N_{2a} + N_{3a} = [N_1 + N_2 + N_3 - (N_{2t} + N_{3t})]\ \tau_a\ C3 \qquad (A4)$$

The resulting true coincidence-anticoincidence rates are therefore:

$$N_{3t} = N_3 - \frac{N_2\ \tau_a\ C2}{1 - \tau_a\ C2} \qquad (A5)$$

$$N_{2t} = \frac{N_2}{1 - \tau_a\ C2} - \frac{N_1\ \tau_a\ C3}{1 - \tau_a\ C3} \qquad (A6)$$

The dead time corrections discussed above were applied after the true coincidence rates had been calculated.

Particle fluxes derived from these counting rates depend on the proton energy spectrum because the geometric factor is energy dependent. We did not use HET in one of its designed operating modes, and different path lengths through the stack were possible because the acceptance cone had been increased from 29° to ~ 113°. Because the flux decreases with increasing energy, the upper energy cut-off is less important than the energy threshold which can be determined more accurately. The energy ranges and geometric factors shown in Table 1 are based on the following considerations. The lower energy threshold corresponds to just triggering the last detector of the stack for a particle trajectory at ~ 25° to the detector axis. The upper threshold corresponds to the highest energy proton with a high enough dE/dx to still trigger B2.

In the quadruple coincidence mode (B2 C4 C3 C2) forward and backward moving particles fall into different energy ranges because of differences in shielding on the two ends. The geometric factor for forward moving particles is larger because these particles only have to reach the front surface of C2, while backward moving particles have to go through C1 or through the substantially thicker shielding of the side of C2. For triple coincidences,

differences in shielding account for the different energy ranges of particles that come in or go out through the sides. A Monte Carlo calculation of the geometric factor weighted by the particle spectrum would have given more accurate results but was not considered justified in view of the uncertainties associated with the dead time and accidental coincidence corrections.

Fluxes in the energy ranges 48-63 and 63-160 MeV were calculated from triple and quadruple coincidences. Fluxes in the energy ranges given in Table 1 were extrapolated from these two values on the basis of the assumed spectral shape. These fluxes were then used for calculating the effective geometric factor for quadruple coincidences and side corrections for triple coincidences. The calculations were performed reiteratively using power law ($E^{-\gamma}$) or exponential ($\exp - E/E_{CH}$) spectra. The energy range covered is relatively small and the results of the two calculations agreed within a few percent. The errors associated with the 63-160 MeV flux were not increased sigificantly over those of the quadruple coincidence rate; however, because of uncertainties in the correction for high energy particles passing through the sides, the 48-63 MeV flux is considerably less accurate and untrustworthy near the Mimas absorption gap.

As can be seen from Fig. 1, each of the coincidence conditions includes particles with substantially different path lengths through the detectors; therefore, the upper and lower energy thresholds are not sharp. The nominal 48, 63, and 160-MeV threshold energies are not well determined and depend on the shape of the spectrum. Since few corrections have to be made to the 63 to 160-MeV channel, the differential flux shown in Fig. 3 would change approximately proportional to the channel width, and the uncertainty in the width is expected to be less than 30 percent. Because corrections are required for particles penetrating through the sides, the effect of changing

the thresholds of the 48 to 63-MeV channel would be larger than for the 63 to 160-MeV flux. A change in this flux would primarily affect the values of E_{CH} and γ shown in Fig. 4. It is possible that the error bars shown beyond 3 R_S in Fig. 4 are optimistic; however, this does not affect the relative position of the points. A systematic error in E_{CH} would affect the relative phase space density shown in Fig. 7. The overall shape of the curve would not change but the magnitude of the increases and decreases could change.

References

Baum, W. A., T. Kreidl, J. A. Westphal, G. E. Danielson, P. K. Sedelmann, D. Pascu, and D. G. Currie, "Saturn's E ring", Icarus 47, 84-96, 1981.

Birmingham, T. J., "Charged particle motion in the distended magnetospheres of Jupiter and Saturn", J. Geophys. Res., 87, 7421-7430, 1982.

Blake, J. B., H. H. Hilton, and S. M. Margolis, "On the injection of cosmic ray secondaries into the inner Saturnian magnetosphere: I, protons from the CRAND process", J. Geophys. Res. 88, 803-807, 1983.

Connerney, J. E. P., N. F. Ness, and M. H. Acuña, "Zonal harmonic model of Saturn's magnetic field from Voyager 1 and 2 observations", Nature, 297, 44-46, 1982.

Cooper, J. F. and J. A. Simpson, "Sources of high-energy protons in Saturn's magnetosphere", J. Geophys. Res. 85, 5793-5802, 1980.

Fillius, W. and C. McIlwain, "Very energetic protons in Saturn's radiation belt", J. Geophys. Res. 85, 5803-5811, 1980.

Fillius, W., W. H. Ip, and C. E. McIlwain, "Trapped radiation belts of Saturn: first look", Science 207, 425-431, 1980.

Hess, W. N. Chapter 4 in "The radiation belt and magnetosphere", Blaisdell Publsihing Co., 1968.

Krimigis, S. M. and T. P. Armstrong, "Two component proton spectra in the inner Saturnian magnetosphere", Geophys. Res. Lett. 9, 1143-1146, 1982.

Lavine, J. P. and J. I. Vette, "Models of the trapped radiation environment, Vol. VI: high energy protons", NASA SP-3024, 1970.

McDonald, F. B., A. W. Schardt, and J. H. Trainor, "If you've seen one magnetosphere, you haven't seen them all: energetic particle observations in the Saturn magnetosphere", J. Geophys. Res. 85, 5813-5830, 1980.

McKibben, R. B. and J. A. Simpson, "Charged particle diffusion and acceleration in Saturn's radiation belts", J. Geophys. Res. 85, 5773-5783, 1980.

Mead, G. D. and W. H. Hess, "Jupiter's radiation belts and the sweeping effect of its satellites", J. Geophys. Res. 78, 2793-2811, 1973.

Rairden, R., Satellite sweeping of electrons and protons in Saturn's inner magnetosphere", University of Iowa Report 80-29, 1980.

Sauer, H. H., "On Saturn's cosmic ray cutoff rigidities", Geophys. Res. Letters, 7, 215, 1980.

Schulz, M. and L. J. Lanzerotti, "Particle diffusion in the radiation belts", Springer, New York, 1974.

Simpson, J. A., T. S. Bastian, D. L. Chenette, R. B. McKibben, and K. R. Pyle, "The trapped radiations of Saturn and their absorption by satellites and rings", J. Geophys. Res. 85, 5731-5762, 1980.

Simpson, J. A., T. S. Bastian, R. B. McKibben, and K. R. Pyle, "Interim report of the re-examination of the University of Chicago measurements of low-energy proton fluxes in the region 2.3 < L < 4 at Saturn, E.F.I. Preprint No. 81-34, 1981.

Smith, B. A., L. Soderblom, R. Beebe, J. Boyce, G. Briggs, A. Bunker, S. A. Collins, C. J. Hansen, T. V. Johnson, J. L. Mitchell, R. J. Terrile, M. Carr, A. Cook, II, J. Cuzzi, J. B. Pollack, G. E. Danielson, A. Ingersoll, M. E. Davis, G. E. Hunt, H. Masursky, E. Shoemaker, D. Morrison, T. Owen, C. Sagan, J. Veverka, R. Storm, and V. E. Suomi, "Encounter with Saturn: Voyager 1 imaging science results", Science 212, 163-191, 1981.

Smith, B. A., L. S. Soderblom, R. Batson, P. Bridges, J. Inge, H. Masursky, E. Shoemaker, R. Beebe, J. Boyce, G. Briggs, A. Bunker, S. A. Collins, C. J. Hansen, T. V. Johnson, J. L. Mitchell, R. J. Terrile, A. F. Cook, II, J. Cuzzi, J. B. Pollack, G. E. Danielson, A. P. Ingersoll, M. E. Davis, G. E. Hunt, D. Morrison, T. Owen, C. Sagan, J. Veverka, R. Storm, and V. E. Suomi, "A new look at the Saturn system: the Voyager 2 images", Science 215, 504-537, 1982.

Stone, E. C., R. E. Vogt, F. B. McDonald, B. J. Teegarden, J. H. Trainor, J. R. Jokipii, and W. R. Webber, "Cosmic ray investigation for the Voyager mission: energetic particle studies in the outer heliosphere--and beyond", Space Sci. Rev. 21, 355-376, 1977.

Synott, S. P., C. F. Peters, B. A. Smith, and L. A. Morabito, "Orbits of the small satellites of Saturn", Science 212, 191-192, 1981.

Thomsen, M. F., C. K. Goertz, and J. A. Van Allen, "On determining magnetospheric diffusion coefficents from the observed effects of Jupiter's satellite Io", J. Geophys. Res. 82, 5541-5550, 1977.

Thomsen, M. F. and J. A. Van Allen, "Motion of trapped electrons and protons in Saturn's inner magnetosphere", J. Geophys. Res. 85, 5831-5834, 1980.

Van Allen, J. A., B. A. Randall, and M. F. Thomsen, "Sources and sinks of energetic electrons and protons in Saturn's magnetosphere", J. Geophys. Res.", 85, 5679-5694, 1980.

Vogt, R. E., D. L. Chenette, A. C. Cummings, T. L. Garrard, E. C. Stone, A. W. Schardt, J. H. Trainor, N. Lal, and F. B. McDonald, "Energetic particles in Saturn's magnetosphere: Voyager 1 results", Science, 212, 231-234, 1981.

Vogt, R. E., D. L. Chenette, A. C. Cummings, T. L. Garrard, E. C. Stone, A. W. Schardt, J. H. Trainor, N. Lal, and F. B. McDonald, "Energetic particles in Saturn's magnetosphere: Voyager 2 results", Science, 215, 577-582, 1982.

Table 1

	Energy Range (MeV)	Geometric Factor (cm^2 sr)
Quadruple/Coincidences of B2 C4 C3 C2		
Front incident	63 - 160	6.5
Back incident	72 - 180	4.7
Triple Coincidences of B2 C4 C3 with C2 anticoincidence		
Total geometric factor	48 - 63	10.5
Out through the side	63 - 160	2
In through the side	72 - 180	2

Detector Parameters:

Detector	Thickness (mm)	Threshold Energy (MeV)	Area (cm^2)
B2	2	2.16	8
C4	6	5.30	9
C3	6	5.28	9
C2	6	5.29	9

Table 2

Magnetic Cut-off Energies of Dipole Field
(calculated using equations of Sauer, 1980)

Dist. from Saturn (R_S)	Equatorial Field Line Distance* (R_S)	Latitude (Degree)	Proton Energy (MeV)	Alpha Particle Energy (MeV/n)
10.0		22.1	180	31
7.5		24.9	300	82
5.0	6.7	28.9	940	302
3.8	5.0	29.5	1,940	730
2.74	3.05	20.0	5,880	2,570
3.03	3.05	-9.9	5,550	2,410
4.35	5.0	-19.5	1,930	708
5.0	6.1	-22.6	1,200	402
7.50		-27.2	265	73
10		-28.6	84	22

*From the "Z3" field model (Connerney et al., 1982) at distances where that model is applicable. These values correpond to the Equatorial distances shown in Figs. 2 to 7.

Table 3:

Pertinent Periods and Distances for Absorption of 90 MeV Protons by Mimas

Parameter	Symbol	$\theta = 85°$*	$\theta = 75°$*	$\theta = 45°$*
Drift period relative to Mimas	τ_d	10.2 m	10.3 m	11.2 min
Bounce Period	τ_b	4.3 s	4.1 s	4.8 s
Average Absorption time per pass	$\langle t_a \rangle$	0.59 s	0.59 s	0.62 s
Gyroperiod	τ_g	0.098 s		
Radius of Orbit	R	185,500 km	(3.075 R_S)	
Width of Sweeping Region	ΔR‡	7,445 km	(0.123 R_S)	
Gyroradius	ρ	1,905 km	1,847 km	1,352 km
Vertical distance traveled in one gyroperiod	$V_{\parallel}\tau_g$	1,048 km	3,111 km	8,500 km
Radius of Mimas	r	196 km		
Characteristics lifetime (equ. 15)	τ_p	3.1 h	9.6 h	41 h
Lifetime averaged over pitch angles	$\langle \tau_p \rangle_\theta$	47 h		
Lifetime of protons diffusing into the gap (equ. 18)		48 m	2.4 h	8.8 h

* θ is the Equatorial pitch angle
‡ Taken from Mimas coordinates during the Voyager 2 encounter which were made available by JPL

Table 4

The CRAND Source Strength
(63 to 160 MeV) and Theoretical Predictions

Parameter	Inbound	Outbound
Observed Proton Flux ($cm^{-2}s^{-1}sr^{-1}$)	6×10^{-2}	4×10^{-2}
Local Pitch angle	67°	81°
Equatorial Pitch angle	45°	75°
χ (injection efficiency)	0.085	0.14
τ_p (characteristic lifetime)	41h	9.6h
J/τ_p ($cm^{-2}s^{-2}sr^{-1}$) (Proton source strength)	4×10^{-7}	1×10^{-6}
$J\tau_n/\chi\tau_p$ ($cm^{-2}s^{-1}sr^{-1}$) (neutron flux)	5×10^{-3}	8×10^{-3}
CRAND Proton Injection at 65° above 10 MeV ($cm^{-2}s^{-2}sr^{-1}$)*	4×10^{-6}	
CRAND Flux from Rings (neutrons $cm^{-2}s^{-1}sr^{-1}$)#	$\sim 10^{-2}$ and $< 10^{-1}$	
CRAND Flux from Atmosphere (neutrons $cm^{-2}s^{-1}sr^{-1}$)#	10^{-4}	

* Result of Blake et al. (1983) extrapolated to the orbit of Mimas
\# From Cooper and Simpson (1980)

Table 5:

Omni-directional 63-160 MeV Proton Flux and Residence Time

Equatorial Distance (R_S)	Proton Flux ($cm^{-2}s^{-1}$)	Residence Time (Approximate)
2.734	8.2×10^{3}*	30 y
2.80 (G Ring)	3.2×10^{3}**	12 y
3.075 (Mimas)		47 h+
3.33	3.8×10^{2}++	1.4 y

* Within $\pm 2.5 \times 10^{3}$ for angular distribution from $\sin\theta$ to $\sin^5\theta$
** Calculated for the observed angular distribution of $0.4 + \sin\theta$
+ Actual lifetime against absorption calculated from absorption cross section of Mimas
++ Calculated for a $\sin^7\theta$ distribution

Figure Captions

Figure 1. Cross-sections of the B end of the High Energy Telescope. The Si detectors labeled A are 0.15 mm thick, B = 2 mm, and C = 3 mm each. The insulators were made of delrin (labeled DEL.), and screws that hold the telescope together are not shown. In Saturn's inner magnetosphere, only detector B2 and the cross-hatched parts of the C detectors were active. Detectors B1, C1, and the guard rings around the C detectors were inactive.

Figure 2. Proton counting rates, 96s average, that have been corrected for accidental coincidences and loss due to counter dead time. The R_2 rate, plotted at one-tenth of its value, was due to B2, C4, C3 coincidences with C2 in anti-coincidence; the R_3 rate was due to B2, C4, C3, C2 coincidences and accepted protons entering from either direction. The error bars shown at low counting rates represent statistical fluctuations, and at high rates they represent the uncertainties in the correction. The Z3 model of the magnetic field (Connerney et al., 1982) was used to determine the equatorial distance of field lines going through the spacecraft and to mark the expected position of satellite absorption features. The G ring, Mimas, and Enceladus are identified by G, M, and Enc., respectively.

Figure 3. The flux of energetic protons is shown in two channels, 48-63 MeV and 63-160 MeV. The 48-63 MeV channel is not shown in the Mimas and G ring absorption region because of large uncertainties associated with corrections for protons entering or leaving through the side of detector C3. See caption to Figure 2 for a definition

of the distance scale and satellite identification. The sharp dip near the G ring observed inbound just before peak flux was due to a spacecraft roll maneuver.

Figure 4. The local pitch angles, solid line, were calculated relative to the observed magnetic field (courtesy of the Voyager Magnetometer Team). Equatorial pitch angles shown as dashed lines were calculated from the local angles using the Z3 magnetic field model (Connerney et al. 1982).

Figure 5. Indicies of the proton energy spectra from the inbound (solid dots) and outbound (open circles) passes. The top panel corresponds to a power law representation and the bottom panel to an exponential in energy. The equatorial field line distance is based on the Z3 model.

Figure 6. The value of "n" is shown versus equatorial field line distance for an assumed pitch angle distribution of the form $\sin^n\theta$. The ratio of the inbound to outbound proton flux was used to calculate n; errors become very large near periapsis because of the small difference in the Equatorial pitch angle of the two observations. A 10-point running average was used between 4.6 and 5.5 R_S. Negative values correspond to a dumbbell distribution, zero to an isotropic distribution, and positive values to a pancake distribution. Considering the size of the error bars, values beyond Enceladus are consistent with an isotropic distribution.

Figure 7. Relative phase space density profiles for protons with constant first adiabatic invariant and 90° pitch angles. In view of the small change of the spectral index with distance, it was kept constant with E_{CH} = 40 MeV for the 15 BeV/G curve and E_{CH} = 33 MeV

for the 60 BeV/G curve. Inbound values are plotted with crosses and triangles and outbound values with diamonds and circles. The top panel was calculated assuming a $\sin^2\theta$ pitch angle distribution and the divergence between the inbound and outbound curves shows that the angular distribution is changing. The bottom panel was calculated using a $\sin^n\theta$ distribution where n changes with distance as shown in Figure 6, but local fluctuations had been smoothed out. This guarantees that the inbound and outbound passes coincide and only the outbound pass has been plotted. Typical error bars are shown at different positions. It should be noted that the curves constitute only an upper limit beyond $5R_S$ because of the presence of a substantial cosmic ray component.

Figure 8. Various particle absorption geometries are shown for protons with a gyroradius ρ, a gyroperiod τ_g, a drift velocity V_d, and a velocity component along the field line of $V_\parallel$. The radius of the satellite is denoted by r and the perpendicular distance between the path of the gyrocenter and the center of the satellite by x. (A) With $x < \rho - r$, the satellite moves inside the gyrocircle and absorption occurs at the leading edge of the gyrocircle only for gyrocenter locations along D; a symmetric situation occurs as the satellite emerges from the gyrocircle. (B) With $\rho - r < x < \rho + r$, the satellite absorbs continuously between first and last contact over the distance 2D. (C) Protons that mirror off the equator and have the proper gyrophase can skip the satellite vertically if $2r < V_\parallel \tau_g$.

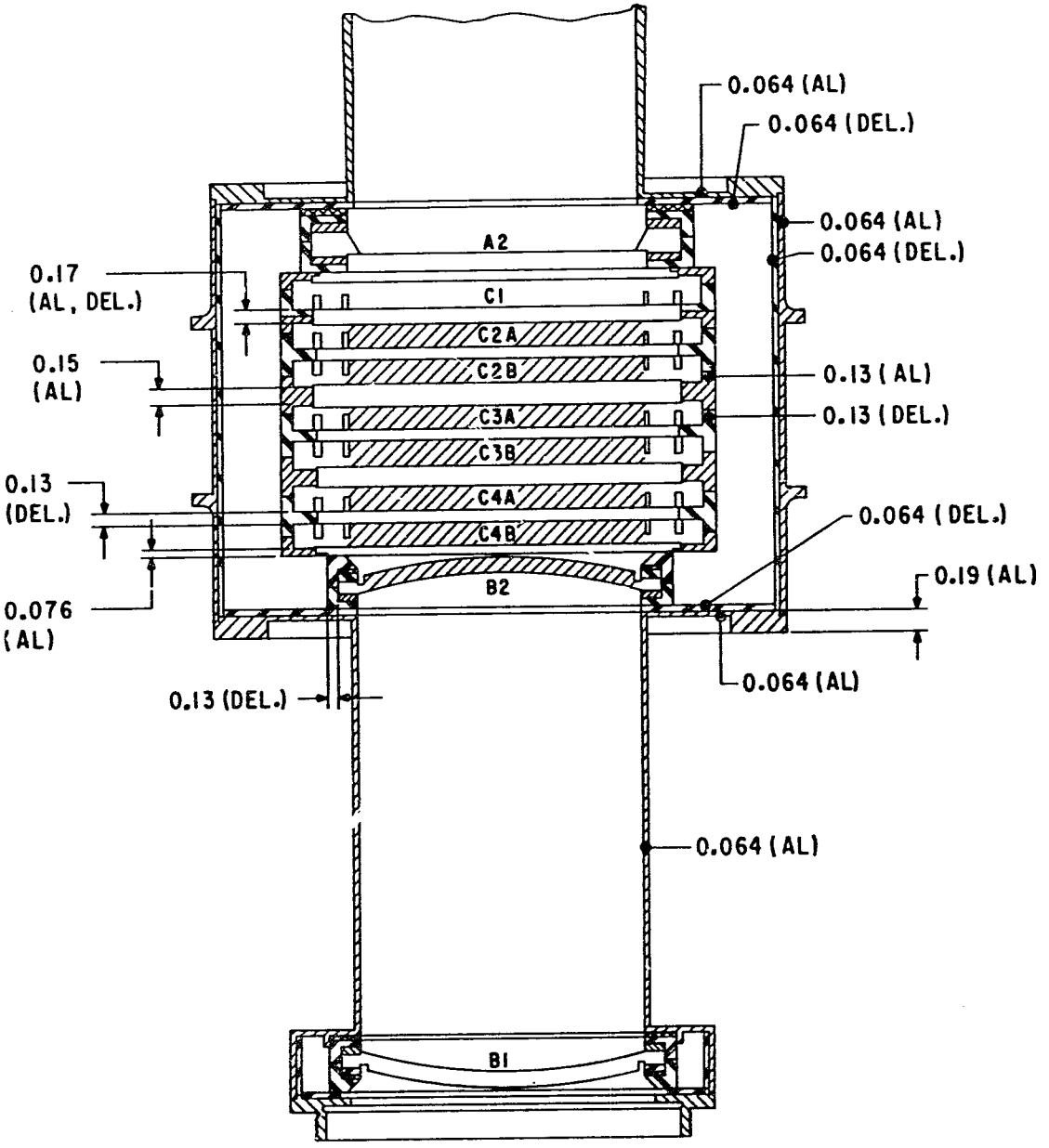

HET TELESCOPE (MJS)

Fig.1

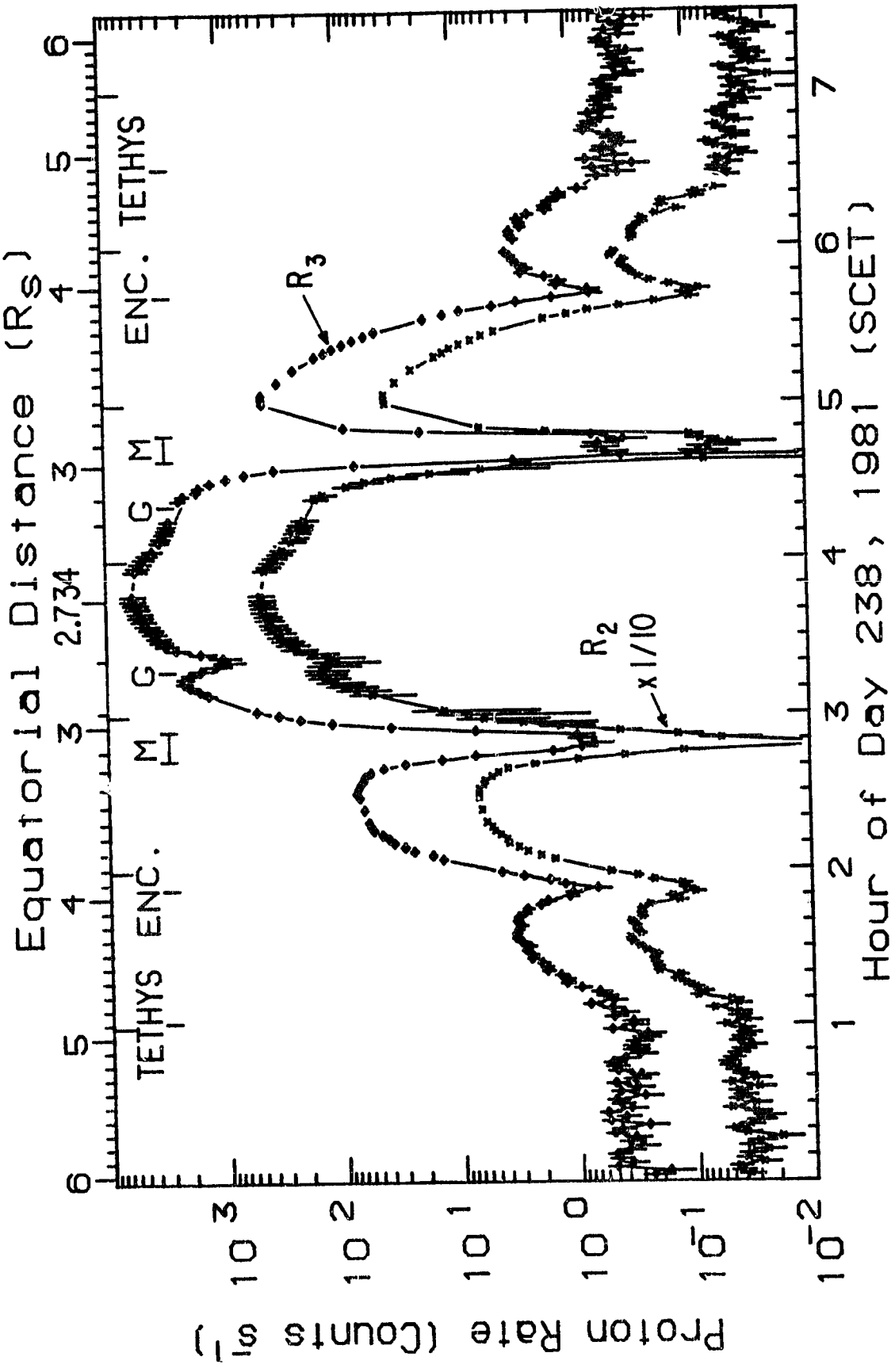

Fig.2

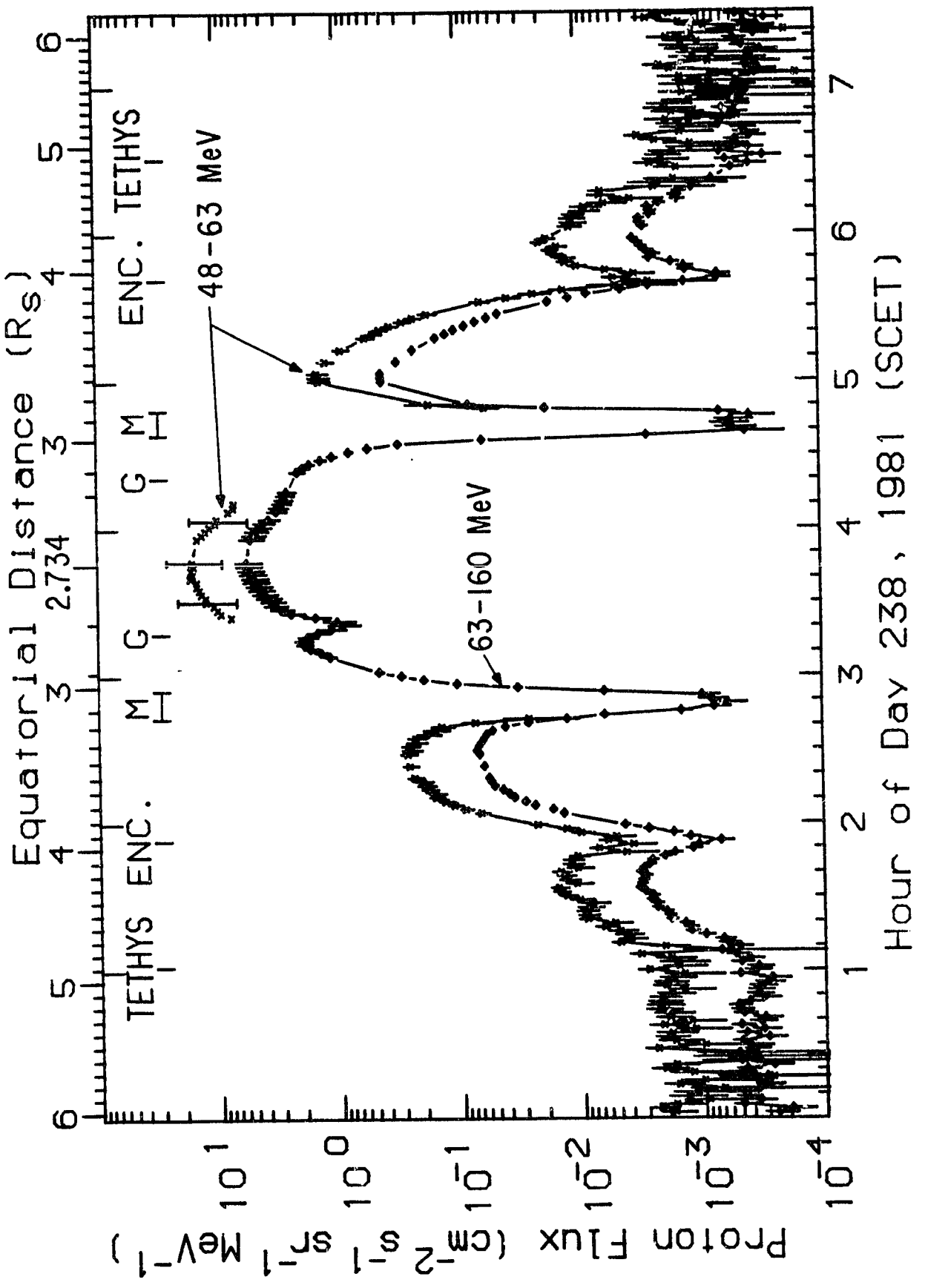

Fig.3

ORIGINAL PAGE IS
OF POOR QUALITY

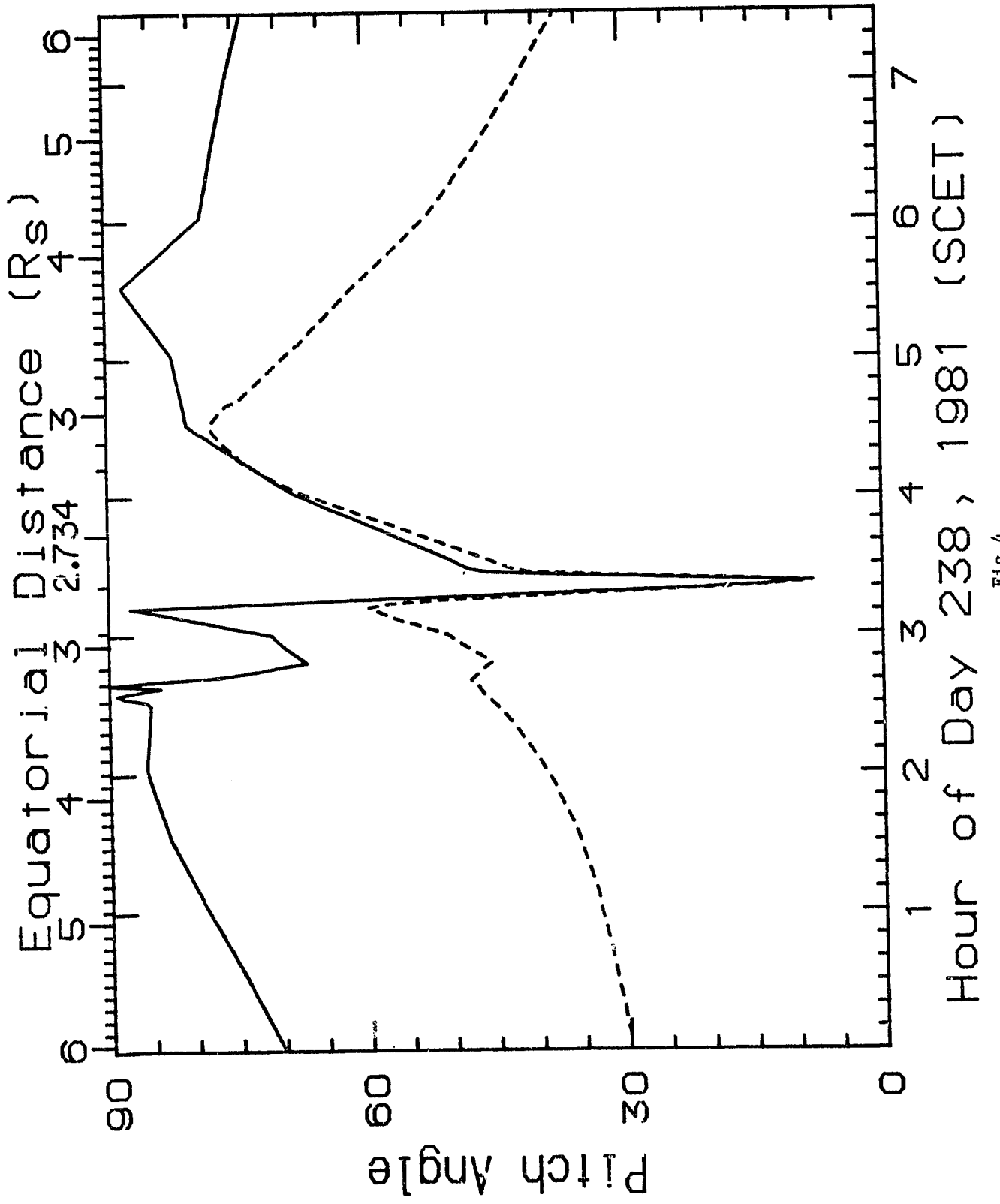

Fig.4

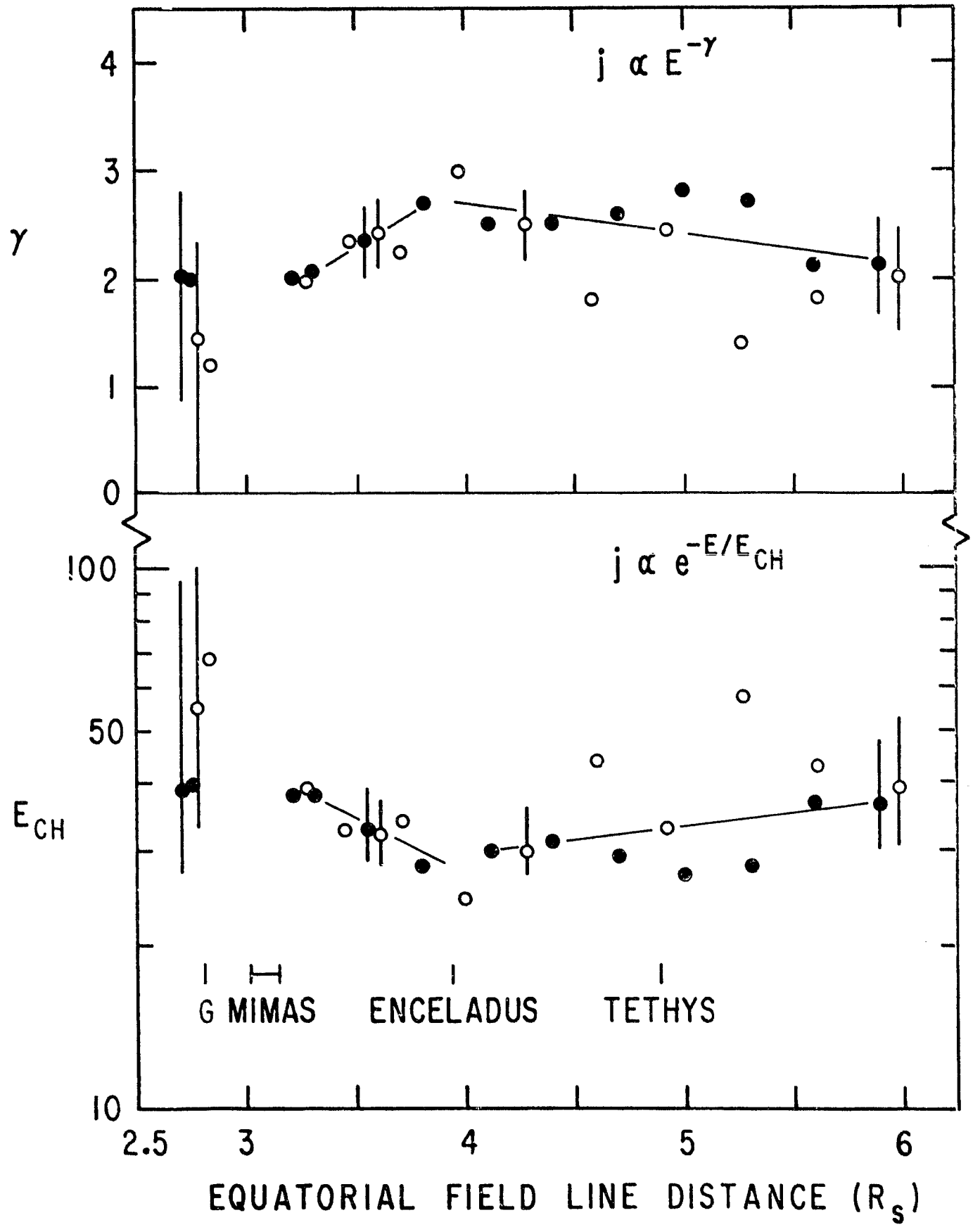

Fig.5

ORIGINAL PAGE IS
OF POOR QUALITY

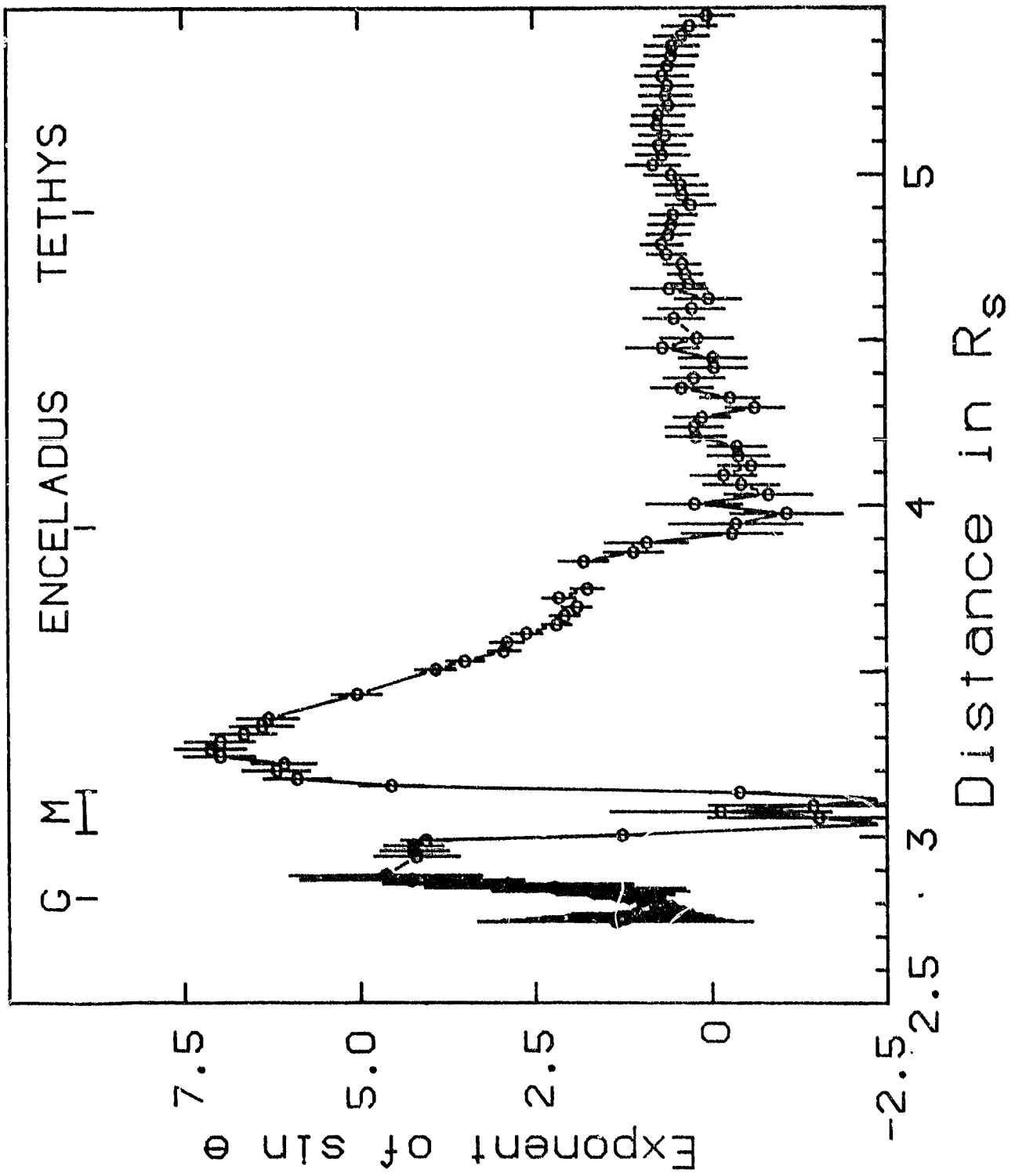

Fig.6

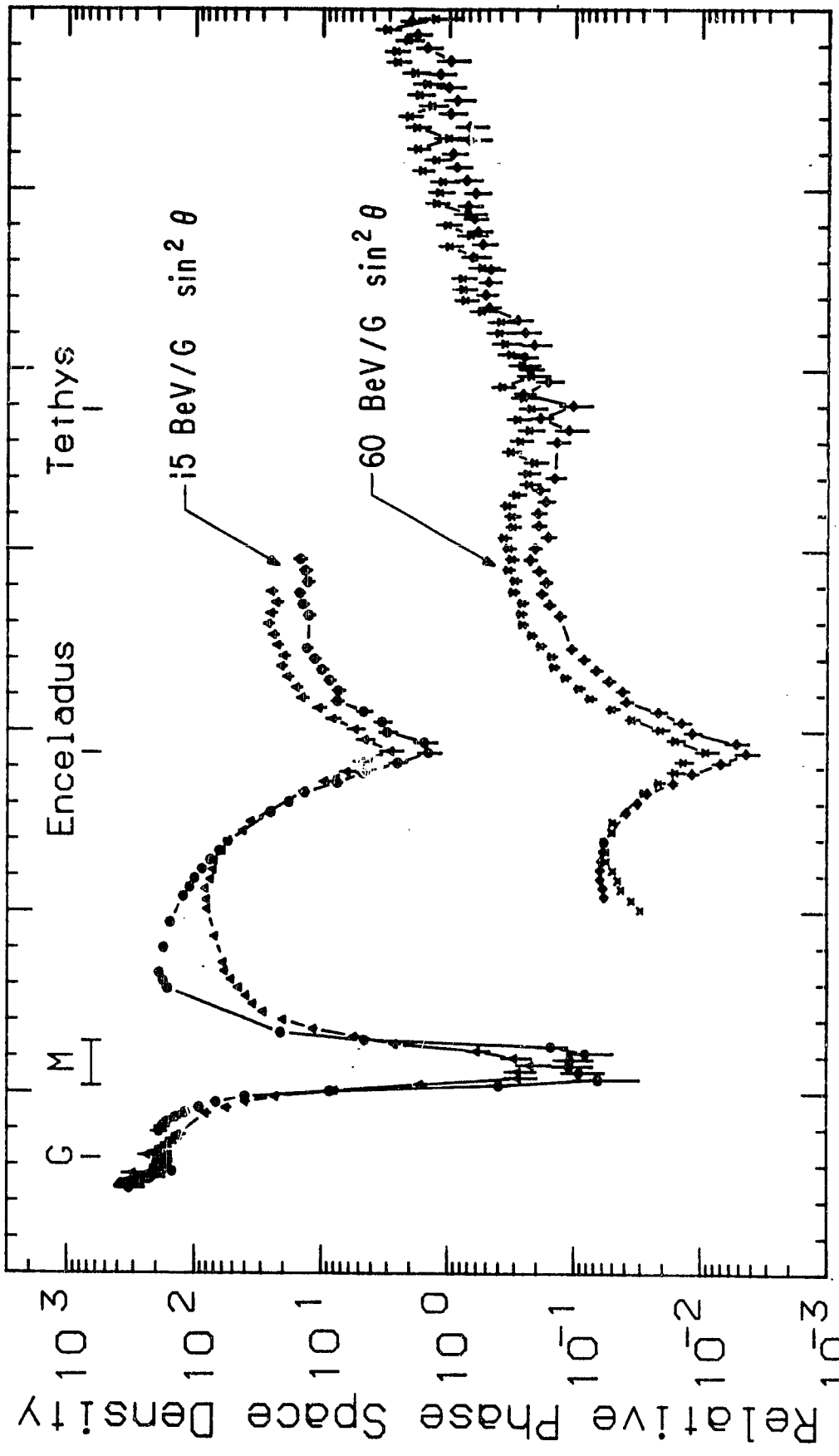

Fig.7a

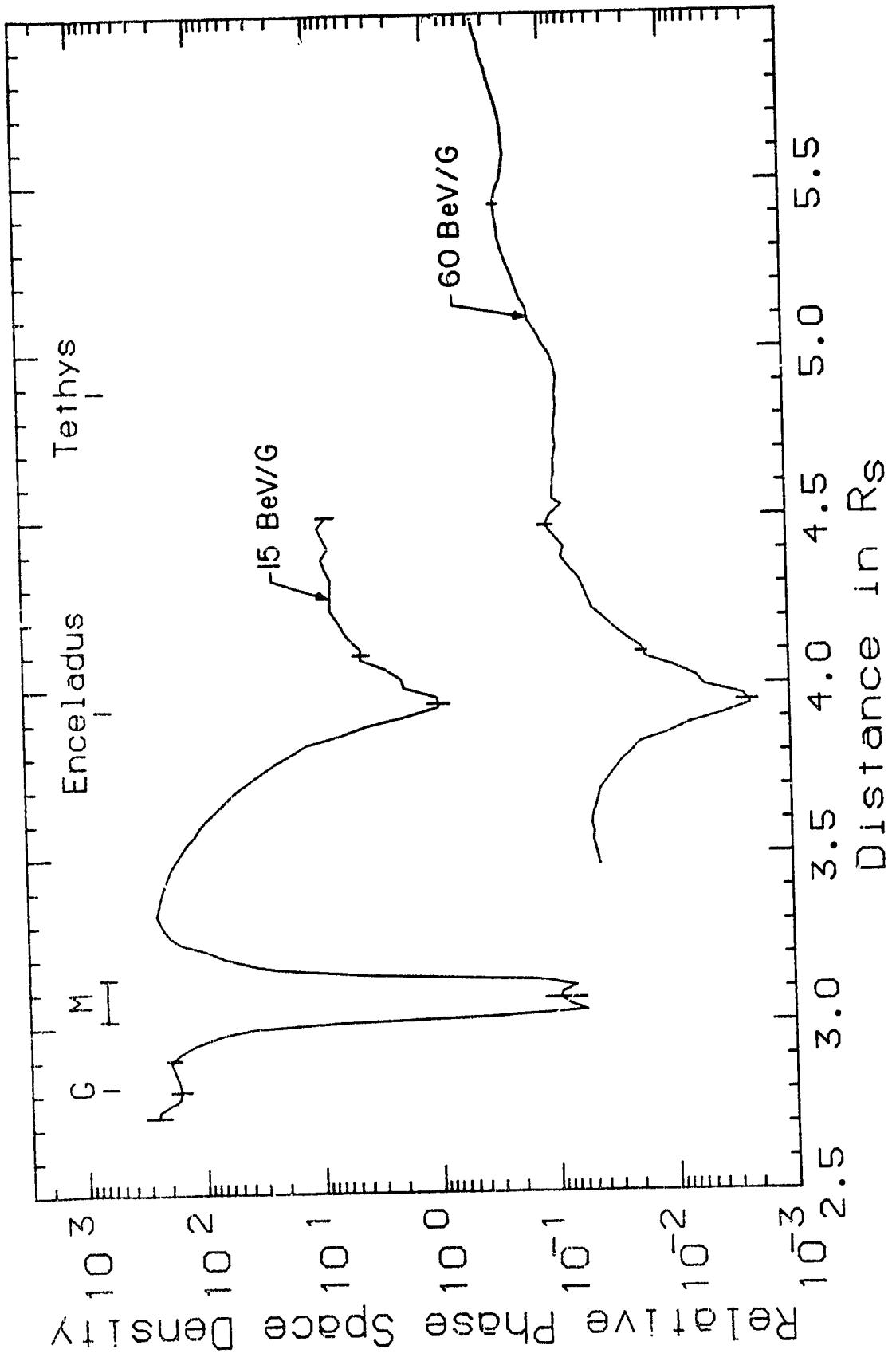

Fig.7b

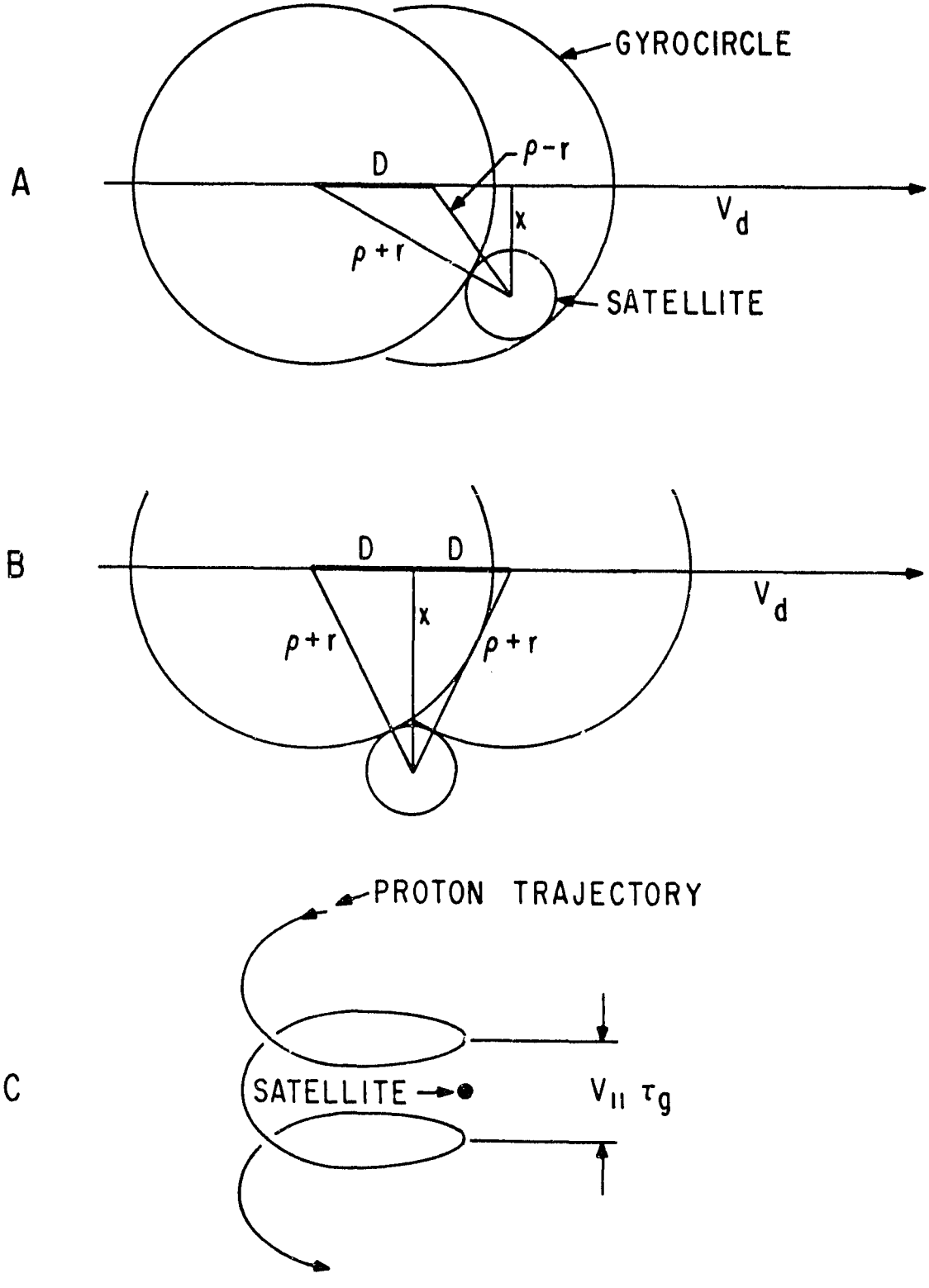

Fig.8